ORIGINAL ARTICLE

Microstructural and mechanical properties of pressureless sintered high-wear-resistant SiC composite materials

R. A. Shishkin[1] · Y. V. Yuferov[1] · R. P. Karagergi[2] · A. V. Schak[3]

Abstract

The microstructural and mechanical properties of pressuless sintered SiC-based composite materials with Al or Cu addition (0–10 wt.%) were studied. The introduction of 1–2 wt.% of metals to the SiC results in appreciable porosity decreases from 31 to $19 \pm 1\%$. Moreover, metallic aids considerably affects the phase composition of the materials. Cu suppresses the formation of mullite. In contrast, Al increases the content of the moissanite phase in the final material because of a thick oxide film on the surface of silicon carbide. However, metal content does not steadily increases due to the melt removes from the open pores during the sintering process. The hardness of the composite material mainly depends on the moissanite phase content, which could be enhanced by metal additives. Developed composite materials have up to 50 and 3 times greater resistance to abrasive and cavitation wear correspondingly than the original porous SiC.

Keywords Silicon carbide · Composite material · Porous ceramics · Wear resistivity · Mechanical properties

1 Introduction

Creating new abrasion, erosion, and cavitation-resistant materials is extremely important in several industries with intense friction of several parts (brake pads) [1–3] or wear by affecting particles and cavitation (cyclones and hydrocyclones) [4–6]. Wear-resistant ceramic materials, such as fused basalt, aluminum oxide, oxide- or nitride-bonded silicon carbide, SiC impregnated with aluminum, and smelted aluminum zirconium silicate ZrO_2–Al_2O_3–SiO_2 are widely used [4–6].

The silicon carbide and aluminum oxide-based materials are the most widespread due to the combination of their high operational and mechanical properties as well as the low cost of the initial powders. The Vickers hardness value (HV10) for compact aluminum oxide ceramics is 1000–1500 [7], for silicon carbide ceramics up to 2500 [8]. However, expensive

manufacturing technologies are required to obtain nonporous wear-resistant ceramics from these materials, such as hot pressing, hot isostatic pressing, and spark plasma sintering [6, 8, 9].

Thus, the development of technologically more ordinary methods for obtaining bulk ceramics has been actively investigated recently [10]. Two main approaches are considered producing dense ceramics: solid-state sintering or application of liquid-phase sintering additives. In the first case, aluminum nitride (AlN) is often used as a widely studied sintering additive [10–15]. Thus, in the paper [14], a solid solution of silicon carbide and aluminum nitride with yttrium oxide sintering aid was obtained. The sample's overall porosity of 0.6% and flexural strength up to 642 MPa. Special attention should be paid to the article [13], where the synthesis of aluminum nitride occurred in situ within sintering of silicon carbide by a carbothermic reduction of alumina in nitrogen atmosphere, which made it possible to obtain the density of the final ceramics up to 99%.

Additives of metal carbides (for example, B_4C) [10, 16, 17] and borides (TiB_2, ZrB_2) [10, 16] are also widely used, increasing the fracture toughness and strength of the samples. An additive worth mentioning is also graphene [18], which significantly increases the mechanical properties of the material, such as crack resistance, bending strength, and hardness.
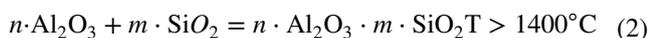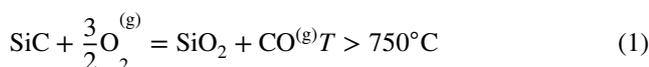
✉ R. A. Shishkin
shishkin@ihim.uran.ru

1 Institute of Solid-State Chemistry Ural Branch of Russian Academy of Science, Yekaterinburg, Russia

2 Research Institute of Nuclear Materials, Joint-Stock Company, Zarechniy, Sverdlovsk region, Russia

3 Ural Federal University, Yekaterinburg, Russia

As a second approach, rare-earth metal oxides are usually used as the liquid-phase sintering aid. The most common among them is yttrium oxide [10, 19–21], which in the presence of aluminum oxide forms the yttrium–aluminum garnets YAG phase ($Al_5Y_3O_{12}$) [10, 20]. Iron oxide (Fe_2O_3) is also considered a possible additive for sintering, making it possible to obtain a material with a relative density of 98% [22]. However, a significant disadvantage of such types of sintering is the enormous temperatures of 1900–2100 °C [10–15, 17–20, 22, 23], which significantly reduces the developed materials' industrial attractiveness.

It was proposed to use an oxide-bonded silicon carbide obtained by sintering the mixture of aluminum oxide and silicon carbide to form mullite bond that results in reducing the cost of manufacturing parts [6]:

$$SiC + \frac{3}{2}O_2^{(g)} = SiO_2 + CO^{(g)} T > 750°C \quad (1)$$

$$n \cdot Al_2O_3 + m \cdot SiO_2 = n \cdot Al_2O_3 \cdot m \cdot SiO_2 \, T > 1400°C \quad (2)$$

Using this low-temperature process results in reducing the cost of manufacturing parts. Nevertheless, the oxide or nitride-bonded silicon carbide produced by pressureless sintering in the temperature range of 1400–1550 °C has a significant porosity of 30–60% and a relatively low bending strength of 7–45 MPa [24–30]. The additives of aluminum hydroxide could be used for increasing the specimens' sinterability. In this case, the additive decomposes to an active form of aluminum oxide during pyrolysis. Also, adding aluminum hydroxide with kaolin [31] or a mixture of calcium fluoride and yttrium oxide [21] was considered for solving the problem. However, the materials obtained using such an approach still have sufficiently high porosity (up to 35%). Even the silicon carbide of different fractions [32] or SiC nanopowder implementation [33] does not entirely solve the issue.

In the paper [34], nickel was deposited on the surface of aluminum oxide, which made it possible to reduce the sintering temperature of the ceramic sample. Unfortunately, it could not completely solve the problem of insufficient bulk properties of pressureless sintered ceramics.

Consequently, it is silicon carbide-based composites could be considered a more promising approach to producing high-wear resistivity materials. In such a way in the papers [6, 35, 36], infiltration of silicon carbide with metallic aluminum was proposed to improve the mechanical properties. Because of the melts of aluminum and its alloys [37–44], copper, and alloys based on it [42, 45–47] have an acute wetting angle (high adhesion) to silicon carbide [48–51], they could be considered as a prospective metal matrix for SiC-based composite material.

The creation of composite materials with a metal binder can be carried out by infiltration (as mentioned earlier) or by introducing silicon carbide particles directly into the metal melt, for example, aluminum. Thus, introducing silicon carbide particles into the metal melt makes it possible to obtain a SiC content of up to 25 vol.% [37, 52]. Although with the help of infiltration, it is possible to achieve a SiC content from 50 to 98.5% [40, 44, 53–55].

It is worth noting that the presented works mainly pay attention to such mechanical properties as hardness, compressive and flexural strength, elastic modulus. Still, there is an evident lack in highlighting and researching the abrasive and cavitation wear of the developed materials.

Based on the above, the direct introduction of metal powders into the initial silicon carbide raw feed with the following sintering in an air atmosphere was proposed. Such a process will presumably allow the metal to spread through the pores and fill them during sintering, followed by oxidation and the formation of oxide-bound silicon carbide. That approach makes it possible to obtain increased mechanical properties and improve the wear resistance of materials. Moreover, manufacturing a composite material with a metal binding phase by powder metallurgy methods [56] can be considered as a more straightforward and more technologically advanced way to obtain products of the complex shape.

Based on the above mentioned, this work is devoted to studying the manufacturing technology of SiC/Al and SiC/Cu composite materials by powder metallurgy methods and investigating their structural and mechanical properties to obtain new wear-resistant composite materials.

2 Experimental

2.1 Materials

The powders of silicon carbide (SiC phase purity $\geq$ 93%, main impurities SiO_2 3.4%; Al_2O_3 3.0%; Si 0.6%, 1100 mesh), copper (Cu, 2 N grade, chemical purity $\geq$ 99%, 500 mesh), and aluminum (Al, extra pure grade, chemical purity $\geq$ 98%, 600 mesh) were obtained from a local supplier. Silicon carbide was wet ground in a ball mill for 24 h in an ethyl alcohol 95% environment. The ground product was vacuumed for 12 h at 50 °C to remove the alcohol. The volume ratio of powder, grinding bodies, and the media was maintained: 42% silicon carbide powder, 42% porcelain grinding bodies, 16% ethanol. The gathered data of the initial powders morphology and particle size distribution is shown in Fig. 1.

2.2 Sample preparation

The silicon carbide and metal (copper or aluminum) powders were taken in the required mass ratio (metal content from 0 to 10 wt.%) and mixed in a porcelain

Fig. 1 SEM of raw materials: **a** copper, **b** silicon carbide, **c** aluminum and their particle size distribution **d** copper, **e** silicon carbide, **f** aluminum
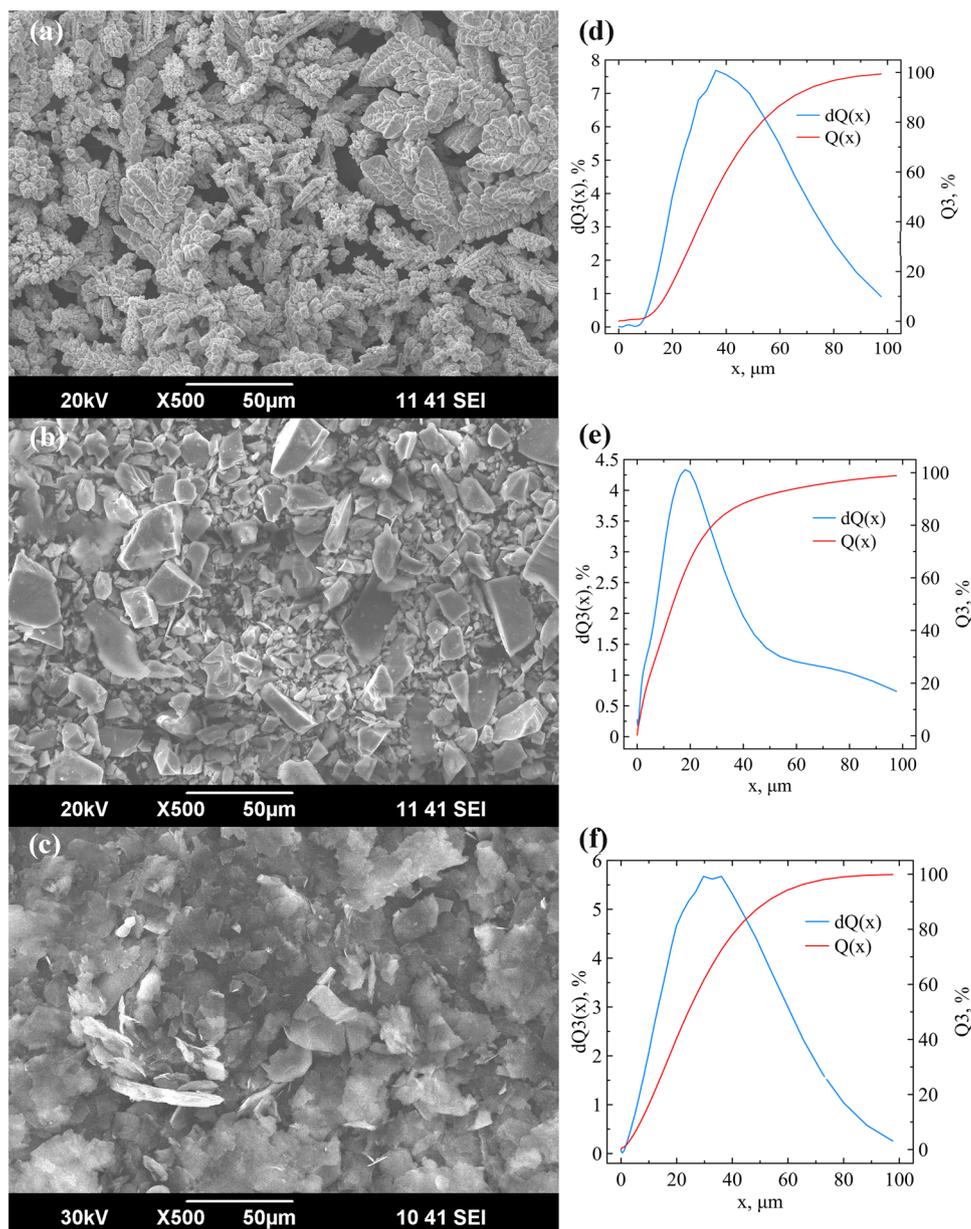
mortar in an ethyl alcohol medium with polyethylene glycol (1 wt.%) for 30 min. The resulting mixture was compacted with a 15 MPa pressure in stainless-steel pellet pressing die and subsequently sintered in Nabertherm Chamber Furnace LHT 08/16 in the air atmosphere in alumina crucible at 1300–1400 °C for 5 h at a heating and cooling rate of 5 °C/min. The obtained samples were tablets with 25 mm in diameter and 4–5 mm height and columns with rectangular cross-section 10×10 mm and a height of 80 mm. The column-like specimens were cut off flat parallel by diamond saw for mechanical testing into two parts: height 60 and 15 mm.

2.3 Experimental setup

The particle size distribution of the initial powders was studied using the Fritsch Analysette 22 MicroTec plus. Before measurement, the samples were put in distilled water and treated with a 100 W ultrasound.

The scanning electrone microscopy (SEM) images were obtained from JEOL JSM 6390LA. Chemical composition and elemental mapping of obtained materials were performed by energy-dispersive X-ray spectroscopy (EDX) using Jeol JED2300 EDX-analyzer of JEOL JSM 6390LA. The sintered tablet form samples were cut by diamond disk, embedded into epoxy resin, and polished to a surface roughness of less than 1 µm.

According to the SEM image, the porosity of the obtained ceramics samples was calculated using ImageJ software [57, 58].

The phase composition and structural studies were conducted using a Shimadzu XRD 7000 diffractometer ($Cu_{K\alpha}$ radiation ($\lambda = 1.5418$ Å) between angles from 10 to 80 degrees, with a step of 0.03 degrees and a shutter speed of 3 s at each point. Diffraction patterns were collected from the polished surface (roughness 100 μm) of the sintered tablet form sample and from the powder obtained by grinding the first one.

The study of mechanical properties was carried out using the Instron 5982 bursting machine. The accuracy of determining the load was 0.5% of the measured value, and the error in determining the deformation of the samples did not exceed ± 0.1 μm. The tests were carried out at room temperature. Specimen with a rectangular cross-section of 10×10 mm and a height of 15 mm were tested to determine the mechanical characteristics during compression. According to the obtained stress–strain curves and the ISO standard [59], the compressive strength was calculated using the Eq. (3), and the elastic modulus (4) was determined between two points measured near the lower and upper limits of the linear section of the stress–strain curve.

$$\sigma_c = \frac{F_{max}}{A_0} \tag{3}$$

where σ_c–comprehensive strength, MPa; F_{max}–maximum compression load, N; A_0—sample cross-sectional area, mm^2.

$$E = \frac{L_0(F_2 - F_1)}{A_0(L_2 - L_1)} 10^{-3} \tag{4}$$

where E–elastic modulus, GPa; L_0 –sample height, mm; F_1, F_2–compression load at certain points, N; L_1, L_2—the longitudinal deformation is appropriate F_1 и F_2, mm.

The flexural strength investigation used a column-like specimen with a cross-section of 10×10 mm and a height of 60 mm. The distance between the supports is 40 mm. According to the stress–strain curves and the ISO standard [59], the strength at three-point bending was calculated using the Eq. (5). The tip movement speed was equal to 0.5 mm/min.

$$\sigma_f = \frac{3F_{max}L}{2bh^2} \tag{5}$$

where σ_f—flexural strength, MPa; F_{max}—maximum load, N; L—the distance between supports, mm; b—sample width, mm; h—sample thickness, mm.

The sintered tablet samples were polished flat parallel. The final dimensions of the specimens, which were analyzed to determine the following properties [4], were a diameter of 25 mm and thickness around 4 mm:

- Bulk density (g/cm^3)

$$\rho = \frac{m}{V} \tag{6}$$

where m is the sample weight and V is the geometric volume;

- Water absorption in a vacuum (percent):

$$V = \frac{m_w}{m_s} \cdot 100 \tag{7}$$

where m_w is the weight of the absorbed water weight and m_s is the weight of the dried sample;

- Open porosity (percent):

$$P = \frac{m_w}{V} \cdot 100 \tag{8}$$

The tablets were weighed (± 0.0001 g), and their dimensions were measured with a thickness gauge (± 0.01 mm). The samples were placed in distilled water and vacuumed in the drying oven for 15 min to achieve maximum water absorption. The weight of pieces was measured to calculate water absorption and porosity (Eqs. 7, 8).

Universal hardness tester ZwickRoell ZHU250 was used to characterize the embedded into epoxy and finely polished samples. Vickers hardness test was performed with square-based pyramid indenter at the applied force value 10 kgf for 12 s. Hardness in HV10 units was calculated on the ZHU250 computing unit by formula (9):

$$HV \approx 0.1891 \frac{F}{d^2} \tag{9}$$

where F is a force in (kgf), d is the average length of the diagonal left by the indenter (mm), measured using a digital ruler of ZHU250.

The abrasive wear study was performed on a custom-made pin-on-disk apparatus according to ASTM G99-17 [60, 61]. The device is an electrical motor that rotates a diamond faceplate (diameter 140 mm, surface roughness 200/160 mesh) at a constant speed of 1468 rpm. A specific holder for the sintered tablets (diameter 25 mm) is installed at a distance of 50 mm from the center of the faceplate. The average pathway length that the piece passes for one complete faceplate turnover is 31.42 cm. A calibrated weight (100 g) is installed on the sample in the holder to create the necessary pressure. The average size of the diamond grains on the diamond faceplate surface is 136 μm. The test time is 15 min, corresponding to a run of about 692 km. During the rotation of the diamond faceplate, distilled water as a lubricant is supplied to its

surface to remove wear products. The scheme of the apparatus is shown in Fig. 2a.

$$W_a = \frac{m_o - m_e}{m_o \cdot S} \qquad (10)$$

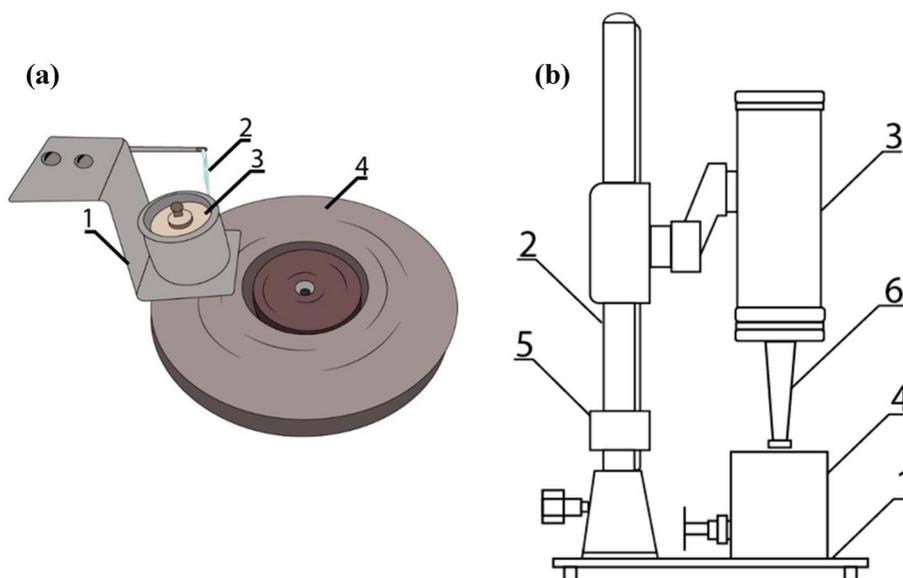$$W_V = \frac{m_o - m_e}{S \cdot \rho} \qquad (11)$$

where W_a and W_v are mass and volume lost after 1000 km run in % and mm^3 consequently, m_o and m_e are mass of the original sample, and after abrasive test, S is the total run of the piece, ρ—is the density of piece.

The study of cavitation wear was carried out according to ASTM G 32 [62–65] on a Techpan Ultrasonic Disintegrator UD-20 automatic type with a frequency of 22 ± 1.65 kHz, an oscillation amplitude at the end of the sonotrode of 16 μm, and a power of 260 W. A tablet sample with a diameter of 25 mm and a height of 5 mm was placed at a distance of 1 mm from the ultrasonic generator. The temperature of the water was maintained at 25 °C. The diameter of the sonotrode was 19.1 mm. The weight of the samples was measured before and after the tests with an accuracy of ± 0.0001 g. The test time was 15 min, after which the change in the sample's mass was recorded. The principal scheme of the device is shown in Fig. 2b.

$$W_{cav} = \frac{m_o - m_e}{m_o \cdot t} \qquad (12)$$

where W_{cav}—is a percent of mass lost per minute after cavitation, m_o and m_e are the mass of the original sample and after cavitation test, t—is the time of the cavitation test.

3 Results and discussion

3.1 Investigation of the phase composition and microstructure of SiC/Cu composite materials

Figure 1 shows the morphology of the initial powders. The shape of the particles is significantly different: SiC particles have an irregular, shattered shape, Cu is dendrites, and Al is flake-like particles.

A temperature of 1400 °C was chosen for sintering as it is a well-known parameter for obtaining oxide-bonded silicon carbide [29, 66, 67]. Figure 3 shows diffractograms of the initial powders and SiC/Cu composite materials and their polished surface, with a copper content in the raw feed varying from 0 to 10 wt.%.

The initial silicon carbide powder comprises moissanite (92.4%) with a small amount of quartz (1.6%), corundum (3%), stishovite (2.4%), and silicon (0.6%). The composition is also confirmed by EDX data: Si $95.6 \pm 0.6\%$, Al $4.4 \pm 0.5\%$. According to XRD, a small content of monovalent copper oxide (Cu_2O, 0.3%) was found in the initial copper powder.

In sintered ceramics, without the addition of copper, the content of the primary phase (moissanite 53.1%) significantly decreases. At the same time, the content of silicon oxides with quartz (4.3%) and cristobalite (18.9%) structures increases. Aluminum impurity passes into two main phases: mullite (14.8%) and kaolinite (9%), formed because of the reaction with amorphous silicon oxide formed during the oxidation of silicon carbide by reaction (1). A sufficiently high porosity explains the decent oxidation of SiC during sintering (open porosity 8.41%, relative density 68.7%). The

Fig. 2 a Pin-on-disk apparatus scheme, 1—sample holder, 2—water, 3—calibrated weight, 4—diamond faceplate **b** UD-20 scheme 1—base; 2—tripod; 3—hub; 4—vessel; 5—thrust ring; 6—sonotrode

Fig. 3 XRD patterns: **a** SiC/Cu composite materials powder, **b** polished sample surface: (1) Copper, (2) SiC powder, (3) sinteted SiC, (4) SiC-1% Cu, (5) SiC-2% Cu, (6) SiC-5% Cu, (7) SiC-10% Cu, (8) SiC-10% Cu 1300 °C; ▼—moissanite (SiC, COD 96-901-0159), ◆—quartz (SiO$_2$, COD 96-900-9667), ●—copper (Cu, COD 96-901-2955), ■—cristobalite (SiO$_2$, COD 96-900-8228), ✶—tenorite (CuO, COD 96-721-2243), ✚—kaolinite (AlSiO$_4$, COD 96-901-5000), ○—mullite (Al$_{4.68}$Si$_{1.32}$O$_{9.66}$, COD 96-900-5503)
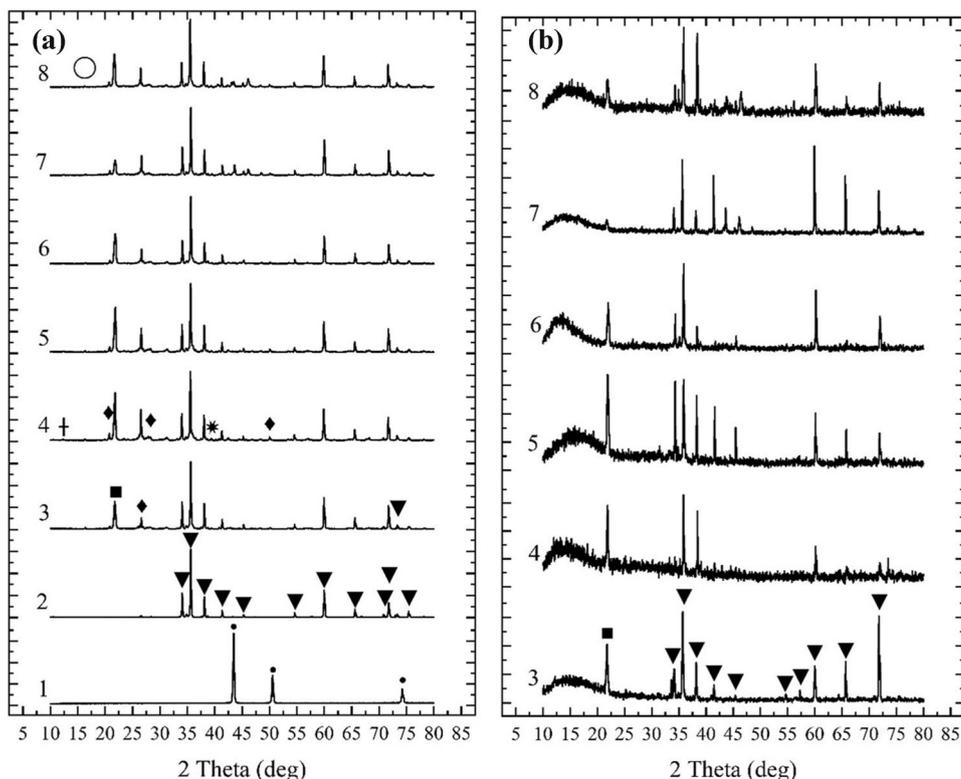
surface of sintered ceramics of silicon carbide is moissanite and cristobalite formed by the oxidation of SiC during sintering [69].

The addition of copper leads to a significant decrease in the kaolinite and mullite amount in the samples. Their average values fluctuate at 6.5 ± 0.5 and $1.5 \pm 0.5\%$, respectively. At the same time, the total content of silicon oxides with the structure of cristobalite and quartz increases from 23.2 to $37.5 \pm 2.5\%$ for all samples with copper content due to covering the surface of silicon carbide particles by melt. It significantly reduces the contact of the resulting silicon oxide and aluminum impurities. It is well-known that copper oxide (CuO) with oxygen conductivity [68] does not prevent further oxidation of silicon carbide after coating its particles with copper.

When SiC is oxidized, an amorphous silicon oxide phase is formed [69], which crystallizes as two modifications: cristobalite and quartz [70]. At temperatures above 1000 °C, the latter can transform into cristobalite [71]. That results in the higher content of the cristobalite phase in samples of $25 \pm 3\%$ versus $11 \pm 2\%$ quartz. The total amount of silicon oxides correlates with the porosity of the samples (the lower the relative density, the higher the content of cristobalite and quartz), which is because of the more complimentary access of oxygen to silicon carbide at high temperatures.

Directly peaks related to metallic copper and copper oxide (CuO) are observed on samples with a content of over

2 wt.% Cu (Fig. 3). The content of copper-containing phases determined by the Rietveld method is maximum (2.8 and 2.4%, respectively for CuO and Cu) at 5 wt.% of copper in the composite. Reduction in the amount of Cu in the sample at 10 wt.% (3.7 and 1.4% for oxide and metal copper, respectively) is associated with the leakage of copper to the sample's surface (Fig. 4), which causes its loss. The appearance of copper on the surface of the specimen is not noticeable on the XRD. However, the content of a large amount of poorly crystallized copper oxide in the surface layers could significantly increase the background in samples with a copper content in the raw feed of over 5 wt.%.

According to XRD, in a sample sintered at 1300 °C, the copper content is only 1.2% as CuO. The lowest relative density amount among all samples (56.0%) explains such due to low sintering temperature. As a result, most copper flowed from the specimen to the surface within the sintering.

There is a decrease in the amount of cristobalite on the polished specimen surface despite the high porosity of samples (5 and 10 wt.% Cu). That could be because of the abundant leakage and coating of the surface of sintered ceramics with copper, which hindered the kinetics of oxidation of silicon carbide.

The appearance of the samples is illustrated in Fig. 4. Traces of metals on the surface are visible when the metal content in the raw feed is over 2 wt.%, which shows the beginning of the outflow of metals to the sample's surface.
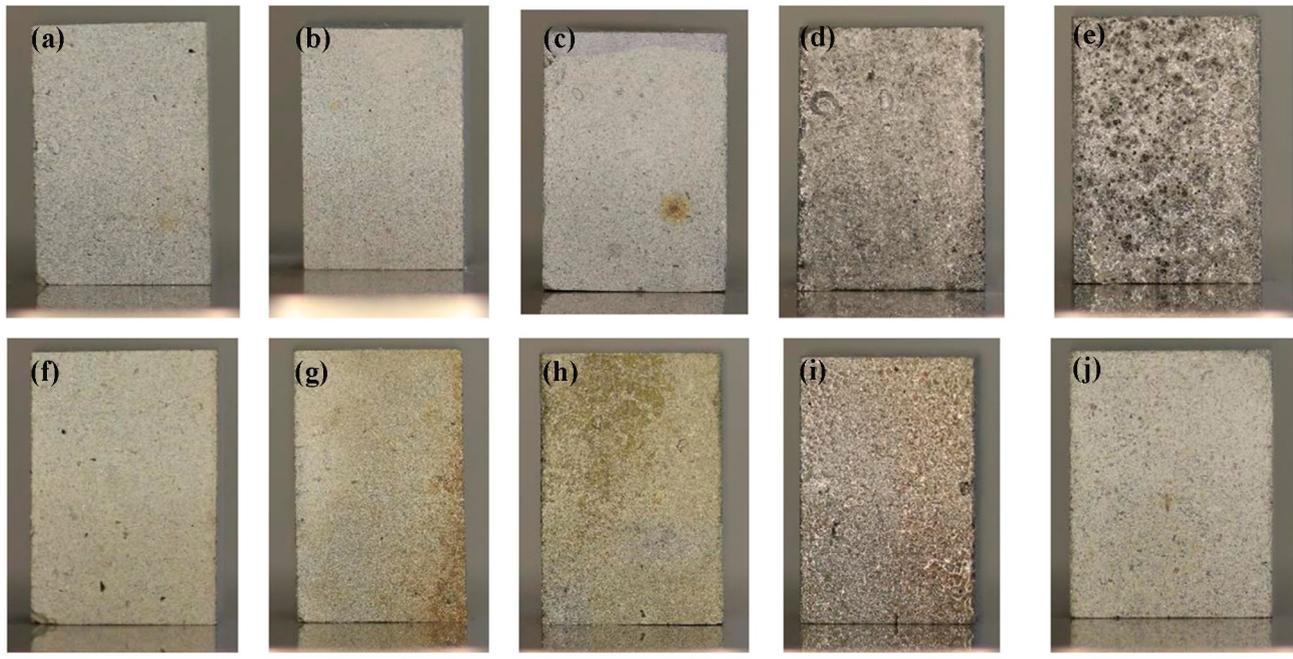
Fig. 4 Images of SiC-based composite materials before compressive test: **a** SiC, **b** 1% Al, **c** 2% Al, **d** 5% Al, **e** 10% Al, **f** 1% Cu, **g** 2% Cu, **h** 5% Cu, **i** 10% Cu, **j** 10% Al-1300 °C

Significant contamination of the surface with aluminum and copper is observed (Fig. 4d, e, h, i), which, as previously noted, leads to an increase in the background XRD of the surface of the samples. Sintered sample with copper additive at 1300 °C had a low density. Moreover, the specimen pressed in a columnar mold significantly changed the geometry and cracked, making it impossible to study its mechanical properties because it will not be presented further.

Figure 5 shows the electron microscopy results of the SiC/Cu composite materials cross-section view, with a variation in the copper content from 1 to 10 wt.%.

The EDX analysis data of the images presented in Fig. 5 are outlined in Table 1. The data on the mass content of metals have been adjusted, considering that silicon is present as carbide and oxide (in a weight ratio calculated from X-ray diffraction data). The average mass content of aluminum impurity (as Al_2O_3, 2.8 wt.%) was introduced in the grinding process of silicon carbide.

Figure 5a shows the microstructure of sintered at 1400 °C silicon carbide without the addition of copper. The SEM image reveals grains of silicon carbide connected through mullite, in which light grains of impurity aluminum oxide are visible. When copper is added to the Fig. 5b–f, the number of light zones related to copper oxide gradually increases. And when 10% Cu is added to the raw feed, large grains related to CuO are visible in the resulting composites. According to the SEM data, the amount of formed mullite for samples with an initial content of 1 and 2% copper is

significantly higher than for other specimens, reducing the resulting porosity. A further increase in the Cu content does not lead to additional compaction of the microstructure.

Elemental analysis performed using EDX shows a higher copper content in sintered SiC/Cu samples at low concentrations: 1.6 and 2.8 wt.%, which offers a relative correlation with the amount of copper powder in the initial compacted material. With the growth of copper amount in the raw feed from 5 to 10 wt.%, Cu content in the composite material gains only from 3.3 to 5.6 wt.% for the sample sintered at 1400 °C, respectively. The leakage of molten copper explains the decrease in the amount of Cu in the composite through the open pores to the sample's surface, which leads to its partial loss because of the acute angle of wetting silicon carbide with copper at sintering temperatures [51]. Higher Cu content in the sample calcined at 1300 °C compared to the same composition obtained at 1400 °C is explained because, with an increase in temperature, the wetting angle of silicon carbide with copper decreases [51] is probably due to a reduction in the melt's viscosity.

The copper leakage from the samples by the porosity calculation is confirmed. The initial sintered SiC, according to the SEM image, has a porosity of 31%, but with introducing 1 wt.% of copper, a significant decrease in porosity to 20.9% is observed. Further addition of copper leads to only a slight reduction in porosity. Increasing Cu content, over 2 wt.% in the raw feed, leads to a rapid rise in porosity to 29.1–34.0%. The sample sintered

Fig. 5 SEM images of Cu-matrix composite material with the Cu content: **a** 0 wt.%, **b** 1 wt.%, **c** 2 wt.%, **d** 5 wt.%, **d** 10 wt.%, **f** 10 wt.% sintered at 1300 °C
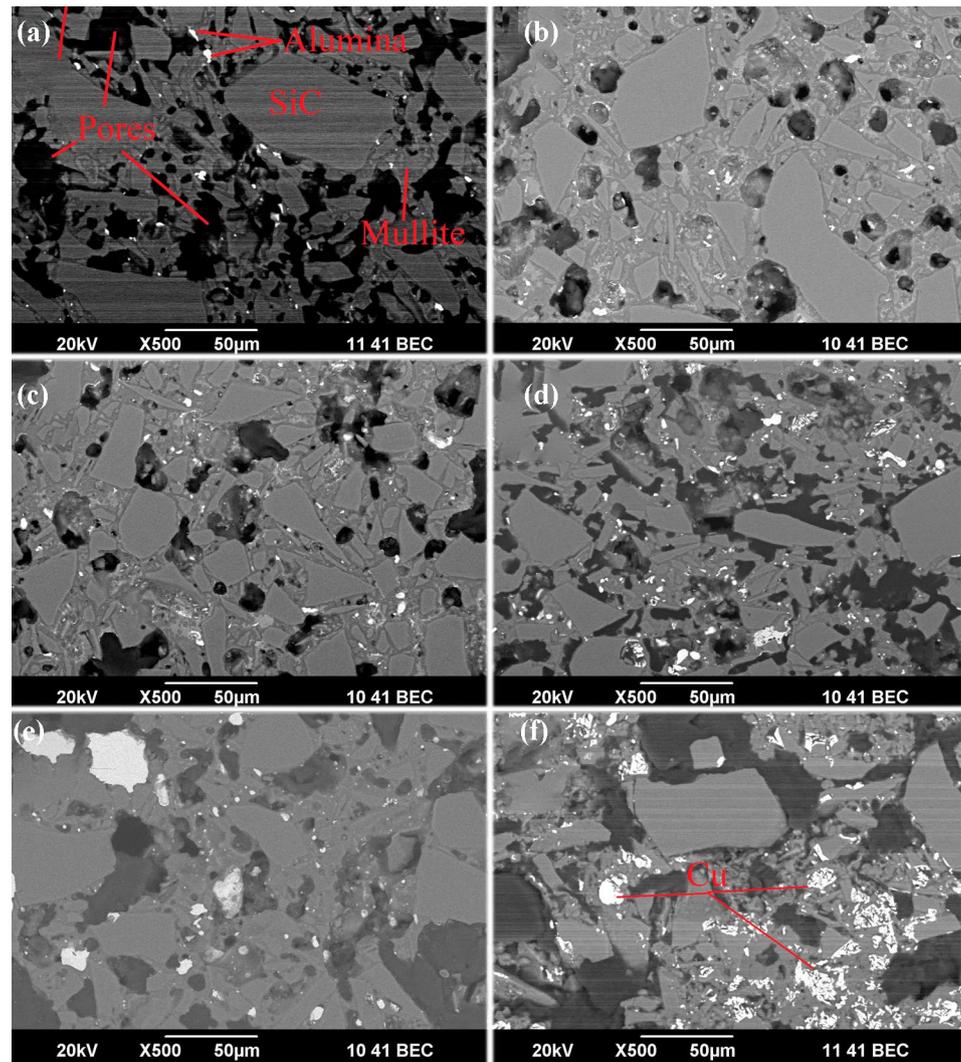

Table 1 The data of EDX analysis of the images shown in Fig. 4 and measurements of open porosity

Sample	Si, wt.%	Cu, wt.%	Al, wt.%	Porosity SEM,%	Density, g/cm^3	Open porosity,%	Water absorption,%
SiC	97.3 ± 0.9	–	2.7 ± 0.6	31.0	2.17	8.41	3.59
1% Cu	95.1 ± 1.5	1.6 ± 0.4	3.3 ± 0.4	20.9	2.08	11.17	5.36
2% Cu	94.4 ± 1.3	2.8 ± 0.6	2.8 ± 0.5	19.7	2.12	2.94	1.39
5% Cu	94.0 ± 2.3	3.3 ± 0.4	2.7 ± 0.5	33.5	2.18	4.03	1.85
10% Cu	91.5 ± 1.5	5.6 ± 0.6	2.9 ± 0.9	29.1	2.29	3.24	1.42
10% Cu-1300 °C	90.4 ± 3.6	7.4 ± 0.7	2.2 ± 0.4	34.0	1.77	7.4	4.17

at 1300 °C enhanced porosity compared to the 1400 °C specimen because of a decrease in the mullite formed by reaction (2). Despite the amplified porosity of the carbide-silicon ceramics, a higher copper content (according to EDX) is observed. The obtained values of open porosity do not explicitly correlate with the calculated ones, which shows the closed nature of the pores or a small fraction of through porosity.

Fig. 6 XRD patterns: **a** SiC/Al composite materials powder, **b** polished sample surface: (1) Aluminum, (2) SiC powder, (3) sinteted SiC, (4) SiC-1% Al, (5) SiC-2% Al, (6) SiC-5% Al, (7) SiC-10% Al, (8) SiC-10% Al 1300 °C: ▼—moissanite (SiC, COD 96–901-0159), ◆—quartz (SiO$_2$, COD 96–900-9667), ●—aluminum (Al, COD 96–900-8461), ■—cristobalite (SiO$_2$, COD 96–900-8228), ✛—kaolinite (AlSiO$_4$, COD 96–901-5000), ○—mullite (Al$_{4.68}$Si$_{1.32}$O$_{9.66}$, COD 96–900-5503), ◇—cordierite (Mg$_2$Al$_4$Si$_5$O$_{18}$, COD 96–900-5803)
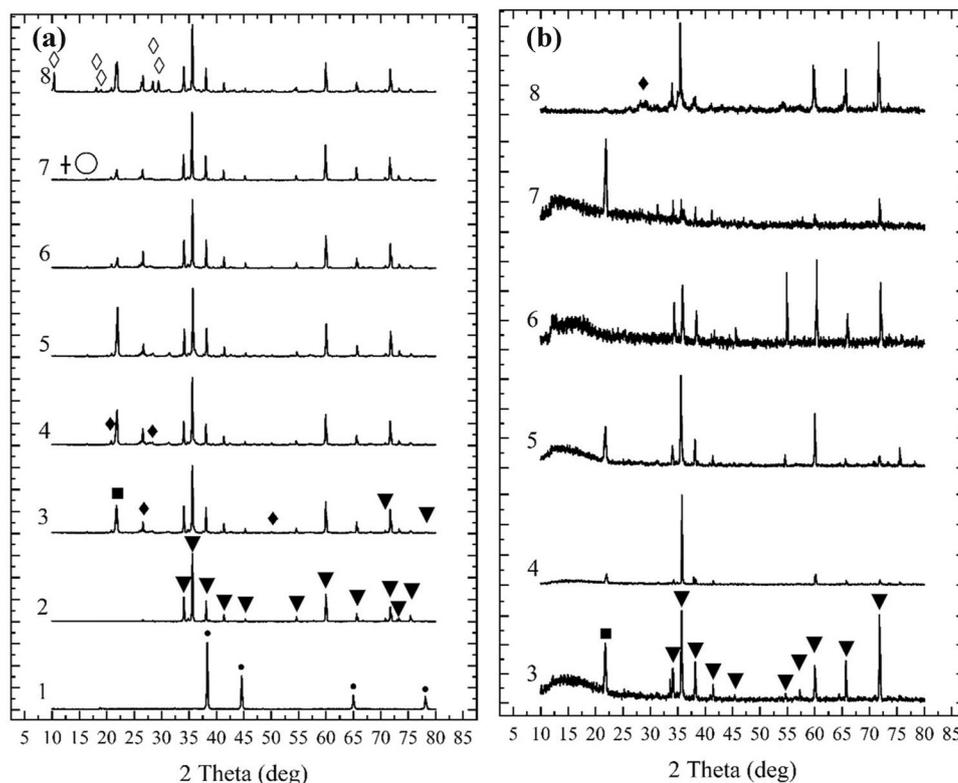
3.2 Investigation of the phase composition and microstructure of SiC–Al composite materials

Figure 6 shows diffractograms of the initial powders, SiC–Al composite materials, and their polished surface, with a variation in the aluminum content in the initial mixture from 0 to 10 wt.%.

Weak peaks of aluminum were recorded on all samples of composite materials, and the content of pure metal fluctuated within the statistical error (0.1–0.4%). The aluminum content is fixed in mullite and kaolinite, the content of which increased from 6.5 ± 0.5 and $1.5 \pm 0.5\%$ to 8.0 ± 1.0 and $3 \pm 0.5\%$, respectively. Raising the metallic aluminum amount in the raw feed, the total proportion of aluminum-containing phases (mullite, kaolinite, and metallic aluminum) increases from 7.0 to 12.1%. As well as for copper, adding aluminum over 5 wt.% in the raw feed is partially lost during sintering, confirmed by the EDX data.

In contrast to SiC/Cu composite materials, the total proportion of silicon oxides in aluminum samples steadily decreases from 34.6 to 22.1%, increasing the aluminum content from 1 to 10 wt.%. This happens due to a thick oxide film formed on the surface of metallic aluminum, which coating silicon carbide grains. Al$_2$O$_3$, unlike CuO, does not pass oxygen, thus preventing the oxidation of SiC. The growing proportion of moissanite also evidences

it in samples from 53.1 to 70.9% for a SiC and composite material SiC-10 wt.% Al, respectively.

The addition of metallic aluminum to the raw feed, unlike copper, is immediately reflected in the elevated background in the XRD patterns of the polished surface of the samples. As in Cu-containing specimens, the most significant proportion of the oxide formed during the oxidation of silicon carbide exists in the form of the cristobalite phase. The ratio of cristobalite to quartz is about 2:1 for all samples. Likewise, in specimens with copper (1–2 wt.%), two main compounds at the sample's surface are observed: moissanite and cristobalite. Interestingly, for SiC-5 wt.% Al, the peak of cristobalite disappears on the polished specimen surface (as for a sintered sample at 1300 °C) but reappears at 10 wt.% Al. As in the copper case, the molten metal flows out onto the surface with the formation of a thick oxide film when an aluminum content is over 5 wt.% in the raw feed. With aluminum, Al$_2$O$_3$ film does not allow oxygen from the air to pass through, which causes a decrease in the amount of oxidized silicon carbide; a similar effect is observed for bulk samples.

A sample of SiC-10% Al is singled out separately, the surface of which, according to XRD, primarily (72.9%) comprises cristobalite. The values obtained are significantly out of step with the results obtained, probably due to sample preparation of the sample surface for XRD.

Fig. 7 SEM images of Cu-matrix composite material with the Al content: **a** 0 wt.%, **b** 1 wt.%, **c** 2 wt.%, **d** 5 wt.%, **e** 10 wt.%, **f** 10 wt.% sintered at 1300 °C
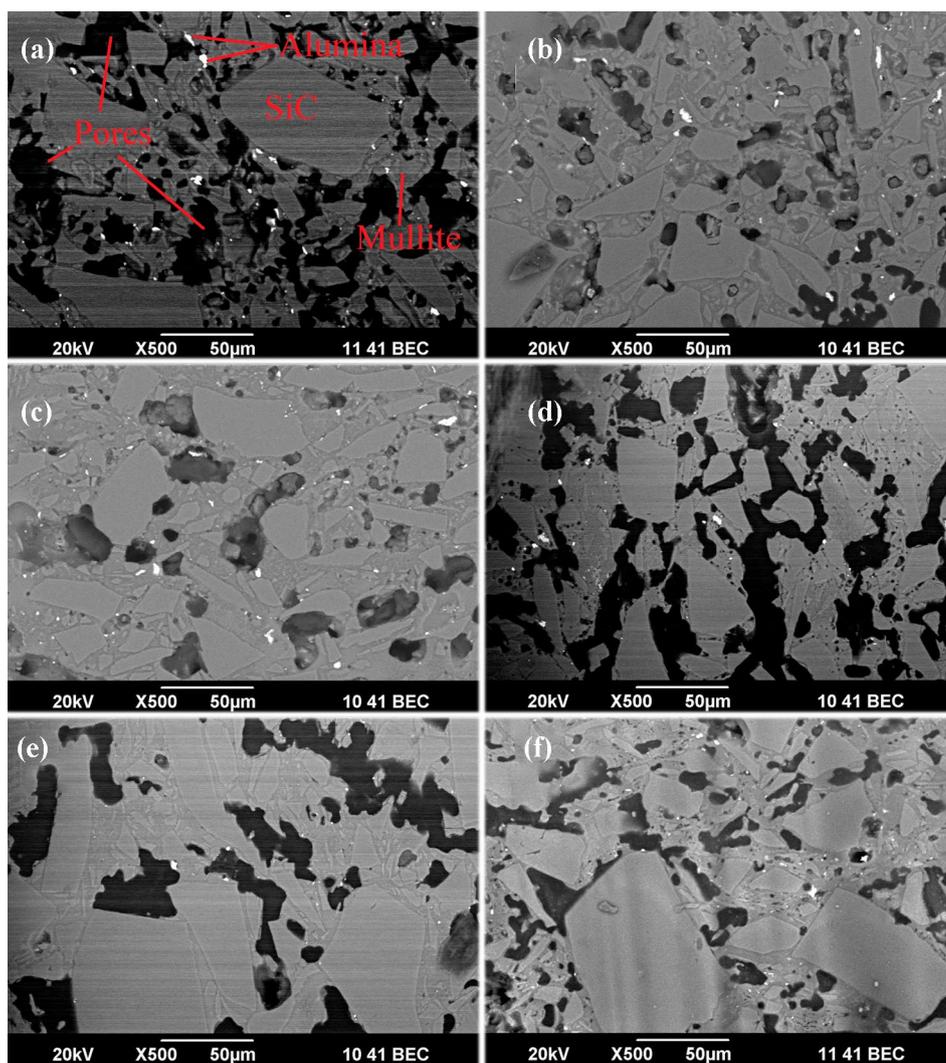
In a sample calcined at 1300 °C, unlike the others, the main phase of silicon oxide is quartz, which has not passed into the high-temperature phase of cristobalite.

Figure 7 illustrates the electron microscopy results of the cross-section view of the composite materials SiC/Al, with a variation of the aluminum content from 1 to 10 wt.%.

Same as in the SiC/Cu series, an immense amount of mullite binder is observed at low concentrations of metallic aluminum additives (1–2 wt.%), which, according to the calculated data, is confirmed by a significant decrease in porosity determined using SEM. With a further increase in the metal content in the charge during sintering of the samples, partial removal of the metal melt occurs, and the formation of many voids between the silicon carbide particles.

The EDX analysis results of the images presented in Fig. 7 are summarized in Table 2. Considering that the

Table 2 The data of EDX analysis of the images shown in Fig. 7 and measurements of open porosity

Sample	Si, wt.%	Al, wt.%	SEM Porosity,%	Density, g/cm³	Open porosity,%	Water absorption,%
1% Al	96.8 ± 1.0	3.2 ± 0.6	19.2	2.16	6.9	3.2
2% Al	96.8 ± 1.3	3.2 ± 0.6	18.7	2.1	8.3	4.0
5% Al	96.2 ± 1.7	3.8 ± 0.8	34.4	2.09	9.2	4.4
10% Al	95.5 ± 2.0	4.5 ± 1.2	26.3	2.30	3.6	1.6
10% Al-1300 °C	93.2 ± 1.4	6.8 ± 1.9	16.3	2.14	13.7	6.4

amount of aluminum introduced as an impurity during grinding, as previously established, is 2.8 wt.%. The added Al content in the obtained samples of the composite material changes from 0.4 to 4.0 wt.%, as the amount of aluminum powder in the raw feed increased from 1 to 10 wt.%. The lower amount of Al in the composite material than the raw feed is explained by its lower viscosity and a sharper wetting angle of silicon carbide than copper [47–50], leading to considerable metal run-out. As in the copper series, a sharp decrease in porosity (SiC 1–2 wt.% Al) and growth with a further enhancement in the metal content because of its leakage during sintering is observed. Also, to the samples with copper, the higher aluminum content in the specimen sintered at 1300 °C is explained by the protective oxide film formation that decreases metal losses. However, due to the significant initial porosity of the composite material, the high value remains. Metallic aluminum due to better adhesion to SiC effectively spread over the entire surface of the voids between the silicon carbide particles. The porosity value determined in the sample SiC-10% Al-1300 °C is the lowest in the considered series of materials. In contrast, SiC/Al 1400 °C samples have more significant porosity value

because of accelerating oxidation aluminum at increasing temperature.

3.3 Investigation of mechanical properties

Figure 8 demonstrates the dependences of the silicon carbide–copper/aluminum composite materials' mechanical properties depending on the mass content of the metal [38, 40–42, 55, 69–76].

There is an almost gradual decrease in the compressive strength of the composite material with an increase in the metal content in the initial feed (Fig. 8a). Reduction of the sample bulk density with the addition of 1 wt.% of copper in the raw feed leads to a sharp drop in compressive strength from 222 to 132 MPa. With a content of 2 wt.%, both the most negligible open porosity and the porosity determined using SEM are observed. Thus, a denser sample has a higher value of compressive strength. A further increase in the copper content entails a decrease in mechanical strength since the copper oxide and silicon oxide obtained during the oxidation process do not form compounds with each other [77]. In contrast, the reduction in compressive strength with the

Fig. 8 Mechanical properties of composite materials: **a** compressive strength, **b** bending strength, **c** elastic modulus, **d** hardness
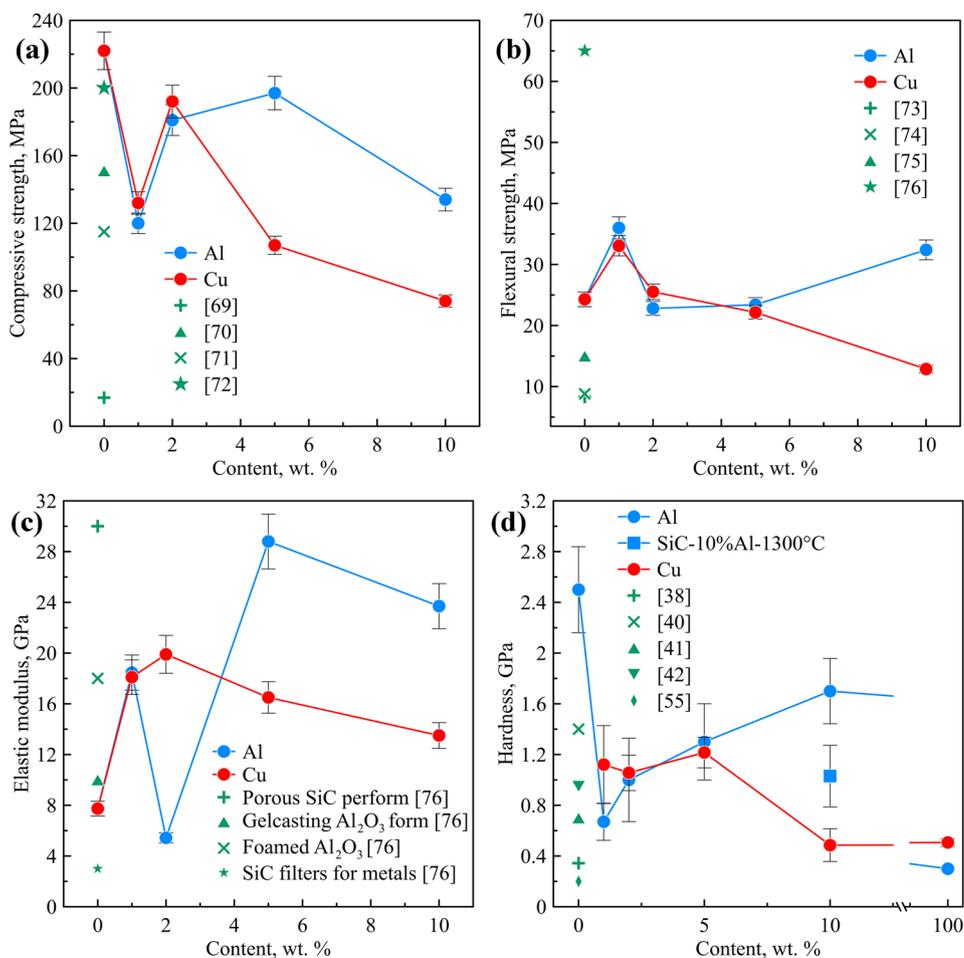
aluminum addition occurs less than copper. This may be because of the oxidation of aluminum and its reaction with silicon oxide, forming oxide-bonded silicon carbide.

Despite the lower porosity, the sample with 1% aluminum to the raw feed and the specimen with copper showed a sharp decrease in compressive strength. This may be due to the high content of the quartz phase (13.3%), while its an amount in SiC (4.3%), SiC-2 wt.% Al (6.6%). A specimen showed a similar value (134 MPa) with 10 wt.% of metallic aluminum in the raw feed, which also has an increased content of quartz phase in the material's volume (11.2%). A similar effect can be noted for samples with copper: an increased quartz content leads to a decrease in the strength of the resulting material.

The compressive strength values for sintered porous silicon carbide are consistent with the data given in the works [69–72]. The variation of the silicon carbide strength obtained values is caused by the difference in the porosity of the materials under consideration.

Flexural strength for all samples (Fig. 8b), except for SiC-10 wt.% Cu, varies between 30 ± 6 MPa. Lower values for silicon carbide with a porosity of about 62% were obtained in papers [73, 74], which is explained by the ceramics' higher porosity. For composite materials with an aluminum additive, the correlation of the measured density of composite materials with their bending strength is observed. The increase in strength for a low copper content is associated with a lessen in the porosity of the composite and higher mechanical properties of copper compared to aluminum. Further decrease in flexural strength when introducing 10 wt.% of copper is caused by the high porosity and the lack of a chemical bond between copper and silicon oxides.

The maximum elastic modulus value was obtained for composites SiC-5 wt.% Al and SiC-2 wt.% Cu (Fig. 8b). The obtained values correspond to industrially used porous materials [76]. For the copper-containing samples, a gradual decrease in elastic modulus occurs over 2 wt.% Cu in raw feed is added. That is associated with increased porosity

and the growth of silicon carbide oxidation. For aluminum-containing samples, the elastic modulus is most influenced by the open porosity of the pieces since the air inclusions represent the second phase with a minimum modulus of elasticity.

The change in the hardness of the obtained composites is shown in Fig. 8d. As the aluminum content in the raw feed rises, the amount of moissanite phase in the final material increases, which leads to a growth in the hardness of composite materials. A similar situation is observed for copper-containing samples, so the lowest moissanite content is kept for a piece with 10 wt.% of the copper in a raw feed. At the same time, in other specimens, SiC content ranges in a narrow range of 56–62%.

3.4 Investigation of abrasive and cavitation wear resistance

Figure 9 demonstrates the results of studies of abrasive and cavitation wear of composite materials. Adding 1–2 wt.% of aluminum or copper led to a substantial enhancement in the abrasive wear resistivity of composite materials, which may be primarily because of a decrease in the porosity of the samples, thereby at each moment, the specific load per unit area reduces, which contributes to a lower wear rate. Further addition of metals leads to an increase in porosity and reduces the amount of mullite, which results in a decrease in abrasive wear resistivity of the samples.

The abrasive wear of porous silicon carbide was 0.21 mm^3 per 1 km of travel, while the lowest values for composite materials were 0.002 mm^3 and 0.010 mm^3 for SiC-2 wt.% Al and SiC-2 wt.% Cu, respectively. Although the obtained hardness values for the initial silicon carbide are higher than for composite materials, it is on this sample that the maximum wear after the test is observed. Moreover, the results of mechanical tests for bulk samples and abrasive wear, where only the surface layers of the piece are examined, do not

Fig. 9 Wear test data: a abrasive, b cavitation
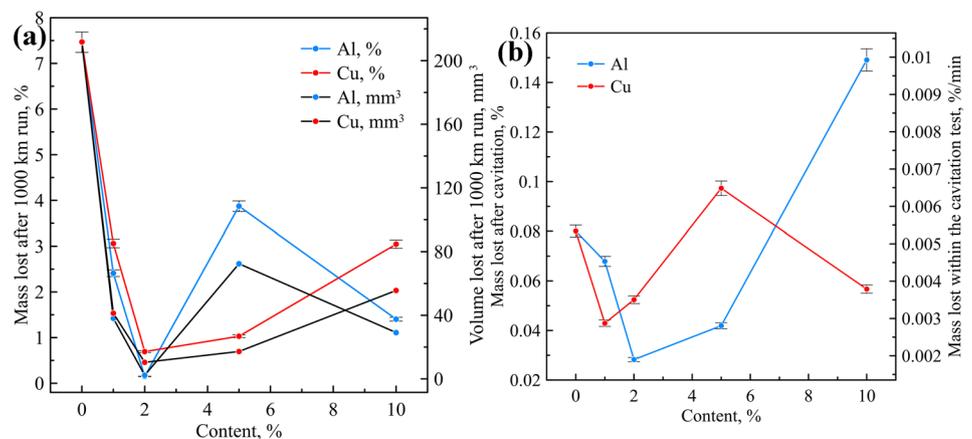
correlate with each other, which may indicate a non-one-horned structure of composite materials.

Cavitation wears largely correlates with the porosity of the obtained materials. An increase in the voids number leads to the generating cavitation bubbles possibility inside the composite material. That leads to the destruction of the surface and the subsurface layers. Small amounts of copper in the raw feed positively affect the sintering of silicon carbide. However, copper is not an effective binder for SiC grains, which leads to a gradual increase in losses during cavitation wear. The deviation of the last sample from the clear trend may be because of the formation of dense large copper oxide grains (as shown at SEM images earlier), which could have a higher resistance to cavitation. In the case of aluminum, the immense amount of mullite binder, according to SEM–EDX data, was formed precisely at a content of 2% in the raw feed, which leads to a decrease in mass loss during testing. Nevertheless, an increase in porosity, together with a reduction in the mullite bond formed amount, reduces the resistance of samples during cavitation.

After cavitation tests, the surface polished during abrasive wear has become dull, which indicates the presence of wear because of the formation of a rough surface. Cavitation wear of composite materials with a metal content of 1–2 wt.% is less than the original silicon carbide (Fig. 9b) due to the combined decrement in porosity and oxide bond content growth. A further increase in the metal content leads to a shift in porosity and cavitation wear. As in the case of abrasive wear, the best result was shown by a composite material with aluminum.

4 Conclusion

Silicon carbide composite materials with addition Al or Cu (in the amount of 0–10 wt.%) in the raw feed were obtained by the pressureless sintering at a temperature of 1400 °C in air.

According to XRD, the main phases of the sintered silicon carbide are moissanite, cristobalite, mullite, and quartz. Porous SiC ceramics are bonded by silicon oxide obtained due to the oxidation of silicon carbide (in case of Cu addition) and mullite (in the addition's case of metallic aluminum). The addition of copper suppresses mullite formation because of its distribution over silicon carbide grains surface during sintering, which preventing the interaction of impurity aluminum oxide and silicon oxide formed as the result of oxidation. Introducing 5 wt.% of Cu into the raw feed sharply decreases the number of oxides formed due to copper leakage to the surface. Copper inhibits the kinetics of oxygen access to the surface SiC grains despite CuO oxygen transport. The number of aluminum-containing phases in the sample volume increases when added metallic aluminum. Same as copper, aluminum flows to the surface during sintering. It forms an oxide film, which, unlike copper,

prevents further oxidation of silicon carbide, thereby increasing the proportion of SiC in the final material.

As a result of studying the samples by the SEM method, it was shown that a mullite bond connects silicon carbide grains, the amount of which is maximum when introduced into the raw feed by 1–2 wt.% metallic aluminum or copper. Moreover, the results of measuring porosity from SEM images showed a significant decrease when adding 1–2 wt.% of metal from 31% for the initial SiC to 18.7 and 19.7% for SiC-2 wt.% Al and SiC-2 wt.% Cu, respectively. A further increase in the metal content in the raw feed leads to its leakage from the pores during sintering. As a result, a decrease in the aluminum/copper content in the sintered sample and an enrichment in porosity.

It was found that the samples' density and the quartz phase's content affect their compressive strength. For composite materials with aluminum in raw feed, the latter is fully correlated with their strength. The highest values of compressive strength for composite materials were obtained for samples with 2 wt.% copper (192 MPa) and 5 wt.% aluminum (197 MPa). For pieces with metallic aluminum and copper additives, the maximum flexural strength was 36 and 33 MPa. The obtained values are correlated with the porosity and the amount of mullite bond in the samples. The best values of the elastic modulus were obtained for samples with minimal open porosity. The hardness of composite materials samples is primarily related to the content of the moissanite phase in the specimens.

The results of abrasive and cavitation tests reveal that because of minor additives of metals in the raw feed (up to 2 wt.%), abrasive and cavitation resistance increases by 10–50 and 2–3 times, respectively. Both methods of wear resistivity studying are primarily related to the obtained materials' porosity; thus, the minor additives of metals in the raw feed contribute to a significant increase in their operational parameters.

Owing to the considerable improvement in functional properties, silicon carbide composite materials with Al or Cu addition (0–10 wt.%) can be considered prospective wear-resistant materials.

Declarations

Conflict of interest The authors declare no competing interests.

References

1. P. Xu, Y. Wang, X. Cao, X. Nie, W. Yue, G. Zhang, Ceram. Int. **47**, 3901 (2021)
2. X. Ma, H. Sun, S. Kou, S. Fan, J. Deng, L. Zhang, L. Cheng, Ceram. Int. **47**, 24130 (2021)

3. J. Napiórkowski, K. Olejniczak, Ł Konat, Materials (2021). https://doi.org/10.3390/ma14082043

4. R.A. Shishkin, Y.V. Yuferov, Glass Ceram. **77**, 57 (2020)

5. A. Koning, J. S. Afr. Inst. Min. Metall. **113**, 643 (2003)

6. J. Foster, Key Eng. Mater. **122–124**, 247 (1996)

7. E. Medvedovski, D.D. Marchant, Proc. Biennial Int. Pipeline Conf. **1**, 223 (2000)

8. M. Swain, R.J. Brook, J. Bill, F. Wakai, F. Aldinger, *Handbook of ceramic hard materials* (CRC Press, Boca Raton, 2000)

9. Z. Aygüzer Yaşar, V.A. DeLucca, R.A. Haber, Ceram. Int. **44**, 23248 (2018)

10. M. Khodaei, O. Yaghobizadeh, S.H. Naghavi Alhosseini, S. Esmaeeli, S.R. Mousavi, J. Eur. Ceram. Soc. **39**, 2215 (2019)

11. H. Dehghani, M. Khodaei, O. Yaghobizadeh, N. Ehsani, H.R. Baharvandi, S.H.N. Alhosseini, H. Javi, J. Refract. Met. Hard Mater. (2021). https://doi.org/10.1016/j.ijrmhm.2020.105420

12. Q. Li, Y. Zhang, H. Gong, H. Sun, Y. Zhai, W. Zhu, J. Jing, Prog. Nat. Sci.: Mater. **26**, 90 (2016)

13. B. Su, G. Liu, Z. Huang, H. Liang, X. Liu, Z. Chen, Ceram. Int. **41**, 14172 (2015)

14. S. Kultayeva, Y.W. Kim, Ceram. Int. **46**, 19264 (2020)

15. D.H.A. Besisa, E.M.M. Ewais, E.A.M. Shalaby, A. Usenko, D.V. Kuznetsov, Sol. Energy Mater. Sol. Cells **182**, 302 (2018)

16. C. Xia, S.A. Delbari, Z. Ahmadi, M. Shahedi Asl, M. Ghassemi Kakroudi, Q. van Le, A. Sabahi Namini, M. Mohammadi, M. Shokouhimehr, Ceram. Int. **46**, 29334 (2020)

17. W. Zhang, S. Yamashita, H. Kita, J. Mater. Res. Technol. **9**, 12880 (2020)

18. Q. Li, Y. Zhang, H. Gong, H. Sun, W. Li, L. Ma, Y. Zhang, J. Mater. Sci. Technol. **32**, 633 (2016)

19. S.V. Amrut Raj, D.C. Jana, P. Barick, B.P. Saha, Ceram. Int. **44**, 9221 (2018)

20. H. Liang, X. Yao, J. Zhang, X. Liu, Z. Huang, J. Eur. Ceram. Soc. **34**, 2865 (2014)

21. Z. Li, Z. Chang, X. Liu, W. Zhao, X. Zhang, S. Xiao, Y. Tian, A. Li, G. Han, J. Li, J. Zhang, Ceram. Int. **48**, 4105 (2022)

22. D. Feng, Q. Ren, H. Ru, W. Wang, Y. Jiang, S. Ren, C. Ye, C. Zhang, S. Wang, J. Alloys Compd. **790**, 134 (2019)

23. M. Liu, Y. Yang, Y. Wei, Y. Li, H. Zhang, X. Liu, Z. Huang, Ceram. Int. **45**, 19771 (2019)

24. S. Ding, S. Zhu, Y.P. Zeng, D. Jiang, J. Eur. Ceram. Soc. **27**, 2095 (2007)

25. P. Prigent, M.L. Bouchetou, J. Poirier, E. de Bilbao, E. Blond, Ceram. Int. **38**, 5643 (2012)

26. J.M. Brossard, P. Prigent, J. Poirier, J. Eur. Ceram. Soc. **33**, 2065 (2013)

27. S.Z.A. Bukhari, J.H. Ha, J. Lee, I.H. Song, J. Eur. Ceram. Soc. **38**, 1711 (2018)

28. S.Z.A. Bukhari, J.H. Ha, J. Lee, I.H. Song, Ceram. Int. **44**, 14251 (2018)

29. S. Baitalik, N. Kayal, J. Alloys Compd. **781**, 289 (2019)

30. J.H. She, T. Ohji, S. Kanzaki, J. Eur. Ceram. Soc. **24**, 331 (2004)

31. F. Wang, S. Hao, B. Dong, N. Ke, N.Z. Khan, L. Hao, L. Yin, X. Xu, S. Agathopoulos, J. Alloys Compd. (2022). https://doi.org/10.1016/j.jallcom.2021.162231

32. Y. Li, Y. Ma, Y. Li, S. Li, J Eur Ceram Soc **41**, 7525 (2021)

33. Y.H. Kim, Y.W. Kim, W.S. Seo, J Eur Ceram Soc **40**, 2623 (2020)

34. D. Firoozbakht, S.A. Sajjadi, H. Beygi, H. Sazegaran, Ceram. Int. **44**, 18156 (2018)

35. S. Li, Y. Li, Q. Wang, K. Miao, X. Liang, Z. Lu, D. Li, Ceram. Int. **47**, 24340 (2021)

36. A. Demir, N. Altinkok, Compos. Sci. Technol. **64**, 2067 (2004)

37. J. Kumar, D. Singh, N.S. Kalsi, Mater. Today Proc. **18**, 3218 (2019)

38. J. Chandradass, T. Thirugnanasambandham, P. Jawahar, T.T.M. Kannan, Mater. Today Proc. **45**, 7147 (2020)

39. L.N. Wankhade, D. Rathod, M.R. Nukulwar, E.S. Agrawal, G.R. Chavhan, Mater. Today Proc. **44**, 2740 (2021)

40. A. Zulfia, Adv .Mater. Res. **277**, 21 (2011)

41. R. Kumar Yadav, Z. Hasan, A. Husain Ansari, Mater. Today Proc. **21**, 1537 (2020)

42. J. Singh, C.S. Jawalkar, R.M. Belokar, Silicon **12**, 2433 (2020)

43. M.S. Mhaske, U.M. Shirsat, Mater. Today Proc. **44**, 376 (2021)

44. H. Nakae, Y. Hiramoto, Int. J. Met. (2011). https://doi.org/10.1007/s40962-018-0253-0

45. A. Devaraju, P. Sivasamy, R. Gopi, A. Muthiah, Mater. Today: Proc. **39**, 888 (2021)

46. H.R. Akramifard, M. Shamanian, M. Sabbaghian, M. Esmailzadeh, Mater. Des. **54**, 838 (2014)

47. M.R. Akbarpour, H. Mousa Mirabad, S. Alipour, Ceram. Int. **45**, 3276 (2019)

48. V. Martínez, M. Martínez, S. Ordõnez, O. Ordõnez, F. Castro, J. Mater. Sci. **38**, 4047 (2003)

49. M. Noori, M. Chisamera, H. Faleh, F. Ştefănescu, G. Neagu, Adv. Mater. Res. **1128**, 149 (2015)

50. M.L.A. Graça, C. Cairo, E.E.S. Moraes, M.L.A. Graça, C.A.A. Cairo, 17 Congr Bras. Eng. Cienc. Mater. **15**, 4217 (2006)

51. J. Marín, L. Olivares, S. Ordoñez, V. Martínez, Mater. Sci. Forum **416–418**, 487 (2003)

52. S.V. Nair, J.K. Tien, R.C. Bates, Int. Met. Rev. **30**, 275 (1985)

53. Y. Yu, A. Du, X. Zhao, Y. Fan, R. Ma, S. Li, W. Wang, Y. Cui, X. Cao, Materials (2019). https://doi.org/10.3390/ma12020318

54. T. Ye, Y. Xu, J. Ren, Mater. Sci. Eng. A **753**, 146 (2019)

55. Y. Cui, L. Wang, J. Ren, Chin. J. Aeronaut. **21**, 578 (2008)

56. R. Abhik, V. Umasankar, M.A. Xavior, Procedia Eng. **97**, 941 (2014)

57. M. Haeri, M. Haeri, J. Open Res. Softw. (2015). https://doi.org/10.5334/jors.bn

58. C. Grove, D.A. Jerram, Comput. Geosci. **37**, 1850 (2011)

59. ISO 20504:2019, *Fine ceramics (advanced ceramics, advanced technical ceramics)—mechanical properties of ceramic composites at room temperature—determination of compressive properties* (ISO, Geneva, 2019)

60. J. Salguero, J.M. Vazquez-Martinez, I. del Sol, M. Batista, Materials **11**, 1236 (2018)

61. X.F. Zhang, G.Y. Lee, D. Chen, R.O. Ritchie, L.C. de Jonghe, J. Am. Cer. Soc. **86**, 1370 (2003)

62. H.R. Bakhshandeh, S.R. Allahkaram, A.H. Zabihi, Ultrason. Sonochemistry **56**, 229 (2019)

63. P.J. Liew, J. Yan, T. Kuriyagawa, Int. J. Mach. Tools Manuf. **76**, 13 (2014)

64. M. Szala, T. Hejwowski, Coatings **8**, 254 (2018)

65. M. Szala, M. Walczak, K. Pasierbiewicz, M. Kamiński, Coatings **9**, 340 (2019)

66. D. Das, N. Kayal, Abstr. Int. Conf. Meet. **1**, 3 (2021)

67. D. Das, S. Baitalik, N. Kayal, Int. J. Appl. Ceram. Tec. **17**, 476 (2020)

68. Z. Yu, C. Li, X. Jing, Q. Zhang, Y. Fang, J. Zhao, J. Huang, Energy Fuels **27**, 2703 (2013)

69. B. Zhang, H. Huang, X. Lu, X. Xu, J. Yao, Ceram. Int. **44**, 16589 (2018)

70. H. Wu, Y. Li, Y. Yan, J. Yin, X. Liu, Z. Huang, S.H. Lee, D. Jiang, J. Eur. Ceram. Soc. **34**, 3469 (2014)

71. A. Gómez-Martín, M.P. Orihuela, J.A. Becerra, J. Martínez-Fernández, J. Ramírez-Rico, Mater. Des. **107**, 450 (2016)

72. C. Yong-Seong, K. Young-Wook, Met. Mater. Int. **11**, 351 (2005)

73. W. Chi, D. Jiang, Z. Huang, S. Tan, Ceram. Int. **30**, 869 (2004)

74. J.H. Eom, Y.W. Kim, I.H. Song, J. Eur. Ceram. Soc. **32**, 1283 (2012)
75. S. Kultayeva, Y.W. Kim, I.H. Song, J. Eur. Ceram. Soc. **41**, 4006 (2021)
76. U.M.B. Al-Naib, *Recent advances in porous ceramics* (IntechOpen, London, 2018)
77. L. Xia, Z. Liu, P.A. Taskinen, J. Chem. Thermodyn. **98**, 126 (2016)